Frequency-dependent inductance and winding loss model for gapped foil inductors

Journal Article

Author(s):
Ewald, Thomas (iD); Biela, Jürgen (iD)

Frequency-dependent inductance and winding loss model for gapped foil inductors

Thomas Ewald, *Student Member, IEEE,* Jürgen Biela, *Senior Member, IEEE,*
Email: ewald@hpe.ee.ethz.ch, biela@ethz.ch

Abstract—**For comprehensively optimizing high-frequency foil inductors, calculating the increased inductance and the additional eddy current losses due to a two-dimensional magnetic fringing field caused by air gaps in the centre leg is mandatory. This paper proposes an analytical model that accurately calculates the inductance and the additional eddy current losses in gapped inductors with foil windings. The analytical field expressions are combined into closed-form winding loss and inductance formulas and verified by measurements. Furthermore, the frequency dependency of the inductance due to the shielding effect of the foil conductors is being discussed.**

Index Terms—**Magnetic components, Inductance, Winding losses, Magnetic field, Fringing effect, Shielding effect**

I. INTRODUCTION

MAGNETIC component design is often based on multi-domain models [1] and comprehensive multi-objective optimization [2], to avoid numerous redesigns and keep development time and cost low. Here, accurate mathematical models are crucial. Since several thousand designs are typically calculated during the optimization, models that offer a small computational effort combined with reasonable accuracy are required.

Considering the design of inductors, besides the winding losses also the inductance must be determined, taking into account high-frequency (HF) effects. While the correct inductance is crucial for the operation of the converter system, the losses determine the design, not only of the component, but also of the (cooling) system. High-frequency effects, such as the frequency-dependent non-homogeneous magnetic field distribution in the core window have an impact on the winding losses but also on the inductance. The magnetic field distribution in the core window is influenced by the current in the conductors (including skin, proximity, shielding effects) and the air gaps in the legs (fringing effect).

A. Winding loss calculation in foil conductors

Winding loss calculation in general is a challenging task when a non-ideal magnetic field distribution, deviating from the classical 1D assumption [3], must be considered. Hence, in many cases the field is assumed to be 1D, even when an air gap is present [4]–[6], and the field significantly deviates from the 1D simplification. However, when foil conductors are considered, calculating the 2D magnetic field in the core window of gapped inductors is mandatory, because foil conductors are particularly sensitive to the air gap fringing field [7].

For considering a 2D magnetic field distribution, different per-unit-length winding loss models including an air gap fringing field have been presented. For example, [7], [8] propose semi-numerical models, where numerical or iterative field calculations are performed before the actual loss calculation. In those models, a numerical field calculation is necessary to consider the impact of the conductor current on the 2D magnetic field. However, the numerical evaluation results in extensive execution times, which makes the models usable only to a limited extent in the context of optimizations. [9] considers the attenuation of the 2D magnetic field only in the first conductor and ignores further conductors, which results in an inaccurate loss calculation. [10], [11] replaces all the individual foil conductors in the winding as one solid copper block. With this simplification the actual position of the individual conductors is neglected, introducing errors in the model. Since fast and flexible analytical models are required, other empirical, numerical, or iterative field calculation methods given in the literature are not considered in this paper – please refer to [12] for a more comprehensive listing of winding loss models.

Since the mentioned modelling approaches for the winding loss calculation result in two-dimensional per-unit-length loss densities, a length scaling model to consider the actual length of the winding turns is necessary to obtain the total losses. In the case of gapped inductors, comprehensive modelling of the 3D geometry of the winding is crucial, since the fringing field of the air gaps is locally influencing the magnetic field. Therefore, simple approaches like the typical mean-length-of-a-turn [13] are not sufficiently accurate.
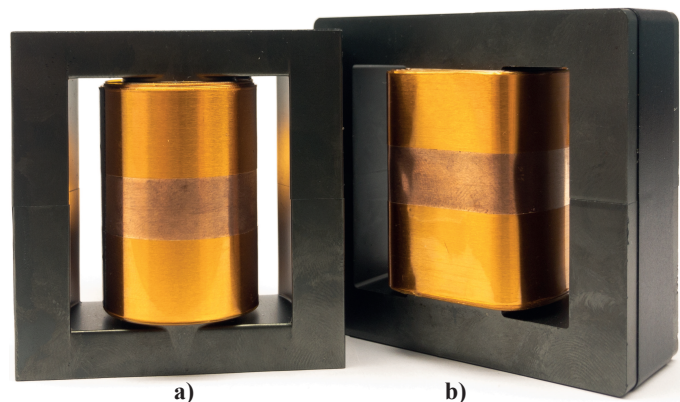

Fig. 1. **a)** Inductor with an ETD 59/31/22 core with circular centre leg. **b)** Inductor with an E 65/32/27 core with rectangular centre leg.

B. Inductance calculation

With the 2D magnetic field formulation in the core window and the air gap, it is also possible to accurately calculate the inductance. However, no approach can be found in the literature, that comprehensively models the winding losses and the inductance of gapped foil wound inductors based on a 2D magnetic field. The reason is, that many 2D magnetic field models use the mirroring method to calculate the magnetic field in the core window (e.g. [7]), which would require numerical integration to obtain the magnetic energy.

Hence, the calculation of the inductance of gapped inductors is usually performed separately with reluctance networks of which the inductance is derived. To consider the influence of air gaps, correction factors for the air gap reluctance are proposed in [14]–[17]. The shielding effect of the foils, which is closely related to the inhomogeneous current density distribution in the foil conductors is known [8], [18], but generally ignored in all inductance models mentioned above. This effect decreases the inductance up to 20% depending on the frequency and therefore counteracts the fringing effect, as will be shown in this paper.

C. Proposed comprehensive modelling

So far, in existing literature no computationally efficient and at the same time sufficiently accurate models are proposed for calculating the winding losses of gapped foil inductors. Furthermore, the shielding effect of foil conductors is ignored in the inductance calculation. Consequently, this paper proposes a new, computationally efficient, and accurate 2D magnetic field formulation and derives the winding losses and the inductance in a quasi-3D model from this 2D magnetic field formulation. This model considers the fringing effect of the air gaps, the skin effect, the proximity effect, as well as the shielding effect of the foils. This results in a comprehensive modelling of the winding losses and the inductance of gapped foil inductors, which is usable in optimization routines.

The paper is organized as follows: Section II proposes an analytical model predicting the two-dimensional, non-homogeneous magnetic field in the core window considering an arbitrary number of air gaps. Section III derives expressions for accurately calculating the inductance and the winding losses of circular symmetric inductors by introducing an accurate length scaling for the 2D models. The adaptation of the model to cores with rectangular centre legs and a finite and complex relative permeability of the core is presented in section IV. The proposed model is verified with FEM simulations and measurements, and the results are discussed in section V.

II. H-FIELD IN 2D CARTESIAN COORDINATES

The following derivations aim for a closed form formulation of the magnetic field and the current density in the core window and the conductors. The analytical solution is obtained by directly solving the Maxwell equations. There, the following assumptions are applied:

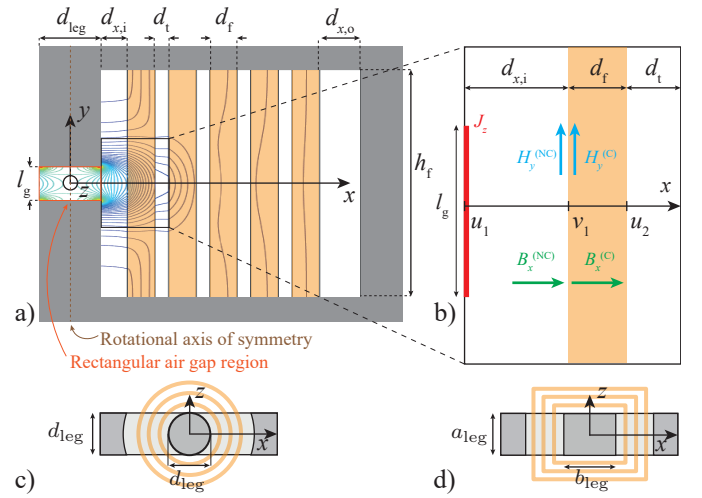1) Core window infinitely long in z-direction: $\rightarrow$ 2D

Fig. 2. **a)** 2D front view of a foil wound E-core inductor, including parameter definition of the 2D model. **b)** Zoomed section of the core window. **c)** Top view of an ETD-Core with circular centre leg. **d)** Top view of an E-Core with rectangular centre leg.

2) Magneto-quasi-static calculations: $\nabla \times \vec{H} = \vec{J}$
3) Harmonic time dependency: $\mathrm{d}/\mathrm{d}t \rightarrow \mathrm{j}\omega$
4) The core material is ideal: $\mu_r \rightarrow \infty$
5) Conductors fill the core window from yoke to yoke

In the following, the fields are derived in 2D Cartesian coordinates. For the sake of brevity, this paper briefly shows the results of the derivations already performed in [12]. The procedure in this paper is to derive the fields in 2D, and to apply a quasi-3D length scaling in section III. This procedure is typical, especially in the winding loss calculation. Errors induced by this procedure are negligible, as shown in [13].

A. Geometrical definitions

The geometry of a 2D core window with foil conductors, including the definition of variables used in the model, is shown in Fig. 2. The window is divided into N rectangular conductors C (copper shaded in Fig. 2), $M = N+1$ non-conductive regions (NC), and the rectangular air gap region (orange rectangle in the centre leg). The conductors have the width d_f, the non-conductive region next to the centre leg (e.g. bobbin) is considered with $d_{x,\mathrm{i}}$, the distance between the conductors is d_t, and the distance between the outermost conductor and the core limb is $d_{x,\mathrm{o}}$. The conductors have the height h_f. The air gap has the length l_g and the centre leg width is d_leg. The origin of the coordinate system is in the middle of the centre leg. The air gaps are assumed to be placed periodically along the y-axis, with symmetry to the x-axis. The number of distributed air gaps is denoted with N_g.

B. Magnetic flux density in the core window

The current, the current density, and the magnetic vector potential are defined to have only components in z-direction. The magnetic field is perpendicular to the magnetic vector potential so that it has only components in the xy-plane. Using the general relation between electric field and magnetic vector potential [19] and interpreting the current density as $\vec{J} = \sigma \vec{E}$

in all regions, with $\sigma = 0$ in the non-conductive regions and $\sigma \neq 0$ in the conductors, results in:

$$\vec{J} = \sigma\vec{E} = -\mathrm{j}\omega\sigma\underbrace{\left(\vec{A} + \frac{1}{\mathrm{j}\omega}\nabla\phi\right)}_{\vec{F}} \tag{1}$$

Here, $\vec{F}$ denotes the modified vector potential, that replaces the magnetic vector potential. As shown in [20], the gradient of the electric potential $\nabla\phi$ inside the conductors has only a z-component, which is constant and can be identified with the voltage drop along the conductor. The modified vector potential is obtained by solving the Laplace and the diffusion equation in the non-conductive regions and the conductors, respectively. This yields:

$$\nabla^2\vec{F}^{(\mathrm{NC})} = 0 \qquad \nabla^2\vec{F}^{(C)} = \gamma^2\vec{F}^{(C)} \tag{2}$$

where $\gamma^2 = \mathrm{j}\omega\sigma\mu$. Here, the modified vector potential in the m-th non-conductive region and the n-th conductor is [12]:

$$\begin{aligned}
F_z^{(\mathrm{NC})} &= C_{m,0}(x-u_m) \\
&+ \sum_{k=1}^{\infty}\left(C_{m,k}\,\mathrm{e}^{-p_k(x-u_m)} + D_{m,k}\,\mathrm{e}^{p_k(x-u_m)}\right)\frac{\cos(p_k y)}{p_k} \\
F_z^{(C)} &= M_{n,0}\,\mathrm{e}^{-\gamma(x-v_n)} + N_{n,0}\,\mathrm{e}^{\gamma(x-v_n)} \\
&+ \sum_{k=1}^{\infty}\left(M_{n,k}\,\mathrm{e}^{-\xi_k(x-v_n)} + N_{n,k}\,\mathrm{e}^{\xi_k(x-v_n)}\right)\frac{\cos(p_k y)}{p_k}
\end{aligned} \tag{3}$$

Substituting (3) into (2), it can be concluded that $\xi_k^2 = \gamma^2 + p_k^2$. u_m and v_n denote the reference coordinate of the respective region (see Fig. 2b). The coefficients indicated with index 0 are called the spatially independent coefficients and the coefficients indicated with index k are called the spatial coefficients. Note, that parts of the solution (all parts containing spatially independent coefficients) are similar to Dowell's model [3], whereas the parts containing the spatially dependent coefficients are added to the model to consider (multiple) air gaps, and are originally derived in [10].

The flux density components for the non-conductive regions and the conductors are calculated with $\vec{B} = \nabla\times\vec{F}$. This results in:

$$\begin{aligned}
B_x^{(\mathrm{NC})} &= -\sum_{k=1}^{\infty}\Big(C_{m,k}\,\mathrm{e}^{-p_k(x-u_m)} \\
&\qquad + D_{m,k}\,\mathrm{e}^{p_k(x-u_m)}\Big)\sin(p_k y) \\
B_x^{(C)} &= -\sum_{k=1}^{\infty}\Big(M_{n,k}\,\mathrm{e}^{-\xi_k(x-v_n)} \\
&\qquad + N_{n,k}\,\mathrm{e}^{\xi_k(x-v_n)}\Big)\sin(p_k y) \\
B_y^{(\mathrm{NC})} &= -C_{m,0} \\
&+ \sum_{k=1}^{\infty}\Big(C_{m,k}\,\mathrm{e}^{-p_k(x-u_m)} - D_{m,k}\,\mathrm{e}^{p_k(x-u_m)}\Big)\cos(p_k y) \\
B_y^{(C)} &= \gamma\Big(M_{n,0}\,\mathrm{e}^{-\gamma(x-v_n)} - N_{n,0}\,\mathrm{e}^{\gamma(x-v_n)}\Big) \\
&+ \sum_{k=1}^{\infty}\alpha_k\Big(M_{n,k}\,\mathrm{e}^{-\xi_k(x-v_n)} - N_{n,k}\,\mathrm{e}^{\xi_k(x-v_n)}\Big)\cos(p_k y)
\end{aligned} \tag{4}$$

where $\alpha_k = \xi_k/p_k$. To satisfy the boundary conditions of the magnetic flux density $B_x(x, -h_\mathrm{f}/2) = B_x(x, h_\mathrm{f}/2) = 0$ it follows that $p_k = 2\pi k N_\mathrm{g}/h_\mathrm{f}$, since the air gaps are placed symmetrically and periocically along the y-axis.

Finally, the magnetic field in the rectangular air gap region (see Fig. 2a) is

$$H_\mathrm{g} = \frac{NI}{N_\mathrm{g}l_\mathrm{g}} \tag{5}$$

and the magnetic flux density $B_\mathrm{g} = \mu_0 H_\mathrm{g}$. The separation between the magnetic field inside the air gap region and the core window is possible because the additional fringing field in the core window can be regarded as a result of additional reluctance paths around the air gaps, that reduce the total reluctance of the magnetic circuit.

C. Coefficients

The following expressions are taken from [12]. The coefficients $C_{m,0}$ for the non-conductive regions are given by:

$$C_{m,0} = \frac{\mu_0(M-m)I}{h_\mathrm{f}} \tag{6}$$

where I is the amplitude of the sinusoidal current. The solution for the coefficients $M_{n,0}$ and $N_{n,0}$ is:

$$\begin{aligned}
M_{n,0} &= \frac{C_{n+1,0} - C_{n,0}\,\mathrm{e}^{\gamma d_\mathrm{f}}}{2\gamma\sinh\gamma d_\mathrm{f}} \\
N_{n,0} &= \frac{C_{n+1,0} - C_{n,0}\,\mathrm{e}^{-\gamma d_\mathrm{f}}}{2\gamma\sinh\gamma d_\mathrm{f}}
\end{aligned} \tag{7}$$

For the spatial coefficients, a system of equations with in total $4N+2$ linearly independent equations can be found for calculating all coefficients $C_{m,k}$, $D_{m,k}$, $M_{n,k}$, and $N_{n,k}$ for each k. For the linear set of equations $\boldsymbol{K}_k\boldsymbol{c}_k = \boldsymbol{b}_k$ the system matrix $\boldsymbol{K}_k$ is given in (9), with $\alpha_k = \xi_k/p_k$, and

$$\begin{aligned}
\boldsymbol{c}_k &= \begin{bmatrix} C_{1,k} & D_{1,k} & M_{1,k} & N_{1,k} & \cdots & D_{(N+1),k} \end{bmatrix} \\
\boldsymbol{b}_k &= \begin{bmatrix} -\frac{2\mu_0 N_\mathrm{g}l_\mathrm{g}H_\mathrm{g}}{h_\mathrm{f}}\,\mathrm{sinc}\left(k\frac{N_\mathrm{g}l_\mathrm{g}}{h_\mathrm{f}}\right) & 0 & \cdots & 0 \end{bmatrix}
\end{aligned} \tag{8}$$

with the normalized *sinc*-function and H_g from (5). With the solution for all coefficients, the 2D magnetic field in the core window and with (1) the 2D current density in the conductors are fully described.

III. LENGTH SCALING OF THE MODEL

In the following, an accurate length scaling for the 2D H-field model from the previous section is developed. For this purpose, a polar system is assumed and the integration in z-direction is replaced by an integration along the circumference. The reason for the integration instead of multiplication with the (individual) turn length is, that the integration in polar coordinates weighs the contribution of each region in the 2D-plane with increasing x (r in polar coordinates) more accurately. This is especially important in the regions close to the air gaps.

$$\boldsymbol{K}_k = \begin{bmatrix} 1 & -1 & 0 & \cdots & & & & & 0 \\ e^{-p_k d_{x,\mathrm{i}}} & e^{p_k d_{x,\mathrm{i}}} & -1 & -1 & 0 & 0 & \cdots & & 0 \\ e^{-p_k d_{x,\mathrm{i}}} & -e^{p_k d_{x,\mathrm{i}}} & -\alpha_k & \alpha_k & 0 & 0 & \cdots & & 0 \\ 0 & 0 & e^{-\xi_k d_{\mathrm{f}}} & e^{\xi_k d_{\mathrm{f}}} & -1 & -1 & 0 & \cdots & 0 \\ 0 & 0 & \alpha_k\, e^{-\xi_k d_{\mathrm{f}}} & -\alpha_k\, e^{\xi_k d_{\mathrm{f}}} & -1 & 1 & 0 & \cdots & 0 \\ 0 & 0 & 0 & 0 & e^{-p_k d_{\mathrm{t}}} & e^{p_k d_{\mathrm{t}}} & -1 & -1 & \vdots \\ 0 & 0 & 0 & 0 & e^{-p_k d_{\mathrm{t}}} & -e^{p_k d_{\mathrm{t}}} & -\alpha_k & \alpha_k & \\ \vdots & & \ddots & & \ddots & & & & \\ 0 & \cdots & & & & 0 & 0 & e^{-p_k d_{x,\mathrm{o}}} & -e^{p_k d_{x,\mathrm{o}}} \end{bmatrix} \tag{9}$$

A. Winding losses and effective resistance

The winding loss is generally determined as [19, sec. 6.9]:

$$P = \frac{1}{2} \iiint x\ \vec{E}\vec{J}^*\ \mathrm{d}x\ \mathrm{d}y\ \mathrm{d}z \tag{10}$$

where $\vec{J}^*$ denotes the complex conjugate of $\vec{J}$. Regarding the integration, all terms containing an integral along y-direction over $\sin(p_k y)$ or $\cos(p_k y)$ vanish. In addition, all those integrals containing $\sin(p_j y)\sin(p_k y)$ or $\cos(p_j y)\cos(p_k y)$ for $j \neq k$ also vanish, due to the orthogonality of the trigonometric functions. With the equations (1) and (3), the winding losses of the n-th conductor are:

$$\begin{aligned} P_n = \pi\omega^2 \sigma h_{\mathrm{f}} \Big(& \zeta_{1,n,0}|M_{n,0}|^2 + \zeta_{2,n,0}|N_{n,0}|^2 \\ & + \Re\left\{\zeta_{3,n,0} M_{n,0} N_{n,0}^*\right\} + \sum_{k=1}^{\infty} \zeta_{1,n,k}|M_{n,k}|^2 \\ & + \zeta_{2,n,k}|N_{n,k}|^2 + \Re\left\{\zeta_{3,n,k} M_{n,k} N_{n,k}^*\right\} \Big) \end{aligned} \tag{11}$$

where $\gamma' = \Re\{\gamma\}$, $\gamma'' = \Im\{\gamma\}$, $\xi_k' = \Re\{\xi_k\}$, $\xi_k'' = \Im\{\xi_k\}$, and

$$\zeta_{1,n,0} = -\frac{(2\gamma'(v_n + d_{\mathrm{f}}) + 1)\,e^{-2\gamma' d_{\mathrm{f}}} - 2\gamma' v_n - 1}{4\gamma'^2}$$

$$\zeta_{2,n,0} = \frac{(2\gamma'(v_n + d_{\mathrm{f}}) - 1)\,e^{2\gamma' d_{\mathrm{f}}} - 2\gamma' v_n + 1}{4\gamma'^2}$$

$$\zeta_{3,n,0} = \frac{(\mathrm{j}2\gamma''(v_n + d_{\mathrm{f}}) + 1)\,e^{-\mathrm{j}2\gamma'' d_{\mathrm{f}}} - \mathrm{j}2\gamma'' v_n - 1}{2\gamma''^2}$$

$$\zeta_{1,n,k} = -\frac{(2\xi_k'(v_n + d_{\mathrm{f}}) + 1)\,e^{-2\xi_k' d_{\mathrm{f}}} - 2\xi_k' v_n - 1}{8p_k^2 \xi_k'^2}$$

$$\zeta_{2,n,k} = \frac{(2\xi_k'(v_n + d_{\mathrm{f}}) - 1)\,e^{2\xi_k' d_{\mathrm{f}}} - 2\xi_k' v_n + 1}{8p_k^2 \xi_k'^2}$$

$$\zeta_{3,n,k} = \frac{(\mathrm{j}2\xi_k''(v_n + d_{\mathrm{f}}) + 1)\,e^{-\mathrm{j}2\xi_k'' d_{\mathrm{f}}} - \mathrm{j}2\xi_k'' v_n - 1}{4p_k^2 \xi_k''^2}$$

The total winding losses are obtained by summing up the individual losses:

$$P = \sum_{n=1}^{N} P_n = \sum_{n=1}^{N} \left(P_{n,0} + \sum_{k=1}^{\infty} P_{n,k} \right) = P_{\mathrm{1D}} + P_{\mathrm{gap}} \tag{12}$$

The expressions (11) and (12) reveal, that the winding losses can be separated into two parts, where P_{1D} consists of all terms indicated with 0 and P_{gap} contains the infinite sum of terms indicated by the index k. The partial losses denoted with P_{1D} are equivalent to [3] and consider the loss contribution of the skin and the layer proximity effect (hence the abbreviation '1D' for 1D layer field), whereas P_{gap} accounts for the additional losses due to the air gap fringing field.

Likewise, the resistance can be separated into two parts, considering the resistance caused by the 1D layer field (resistance increase due to skin and layer proximity effect) and the air gap field, respectively. The frequency-dependent winding resistance is obtained by dividing (12) by the squared current amplitude:

$$R = \frac{2P}{I^2} = R_{\mathrm{1D}} + R_{\mathrm{gap}} \tag{13}$$

This is the total frequency-dependent effective resistance of the inductor, including skin, proximity, and fringing effects. The factor of 2 in the nominator is caused by the fact, that (10) considers the effective value, whereas the current is considered as the amplitude.

B. Magnetic energy and inductance

In addition to the frequency-dependent winding losses the frequency-dependent inductance of the inductor is derived in this paper. In general, the magnetic energy is [19, sec. 6.9]:

$$W = \frac{1}{2} \iiint x\ \vec{B}\vec{H}^*\ \mathrm{d}x\ \mathrm{d}y\ \mathrm{d}z \tag{14}$$

By using (4) the magnetic energy in the m-th non-conductive region and in the n-th conductor is given as:

$$\begin{aligned} W_m^{(\mathrm{NC})} = \frac{\pi h_{\mathrm{f}}}{\mu_0} \bigg(& \frac{(u_m + d_{\mathrm{NC}})^2 - u_m^2}{2}\,|C_{m,0}|^2 \\ & + \sum_{k=1}^{\infty} \beta_{1,m,k}|C_{m,k}|^2 + \beta_{2,m,k}|D_{m,k}|^2 \bigg) \\ W_n^{(\mathrm{C})} = \frac{\pi h_{\mathrm{f}}}{\mu_0} \bigg(& \eta_{1,n,0}|M_{n,0}|^2 + \eta_{2,n,0}|N_{n,0}|^2 \\ & + \Re\left\{\eta_{3,n,0} M_{n,0} N_{n,0}^*\right\} + \sum_{k=1}^{\infty} \eta_{1,n,k}|M_{n,k}|^2 \\ & + \eta_{2,n,k}|N_{n,k}|^2 + \Re\left\{\eta_{3,n,k} M_{n,k} N_{n,k}^*\right\} \bigg) \end{aligned} \tag{15}$$

where d_{NC} is either $d_{x,\mathrm{i}}$, d_{t}, or $d_{x,\mathrm{o}}$,

$$\beta_{1,m,k} = -\frac{(2p_k(u_m + d_{\mathrm{NC}}) + 1)\,\mathrm{e}^{-2p_k d_{\mathrm{NC}}} - 2p_k u_m - 1}{4p_k^2}$$

$$\beta_{2,m,k} = \frac{(2p_k(u_m + d_{\mathrm{NC}}) - 1)\,\mathrm{e}^{2p_k d_{\mathrm{NC}}} - 2p_k u_m + 1}{4p_k^2}$$

and

$$\eta_{1,n,0} = |\gamma|^2 \zeta_{1,n,0} \qquad \eta_{1,n,k} = \left(p_k^2 + |\xi_k|^2\right)\zeta_{1,n,k}$$

$$\eta_{2,n,0} = |\gamma|^2 \zeta_{2,n,0} \qquad \eta_{2,n,k} = \left(p_k^2 + |\xi_k|^2\right)\zeta_{2,n,k}$$

$$\eta_{3,n,0} = -|\gamma|^2 \zeta_{3,n,0} \qquad \eta_{3,n,k} = \left(p_k^2 - |\xi_k|^2\right)\zeta_{3,n,k}$$

The energy stored in the air gap, which contributes the most to the overall inductance, is given as

$$W_{\mathrm{g}} = \frac{\mu_0 \pi d_{\mathrm{leg}}^2 N_{\mathrm{g}} l_{\mathrm{g}}}{8}|H_{\mathrm{g}}|^2$$

which is equal to (14) evaluated in the air gap region with the constant magnetic field from (5). As mentioned, it is assumed that the magnetic field in the air gap is constant and the additional fringing field is fully accounted for by (15).

The inductance of the component is finally derived from the total magnetic energy stored in the core window and in the air gap:

$$L = \frac{2}{I^2}\left(W_{\mathrm{g}} + \sum_{m=1}^{M} W_m^{(\mathrm{NC})} + \sum_{n=1}^{N} W_n^{(\mathrm{C})}\right) \qquad (16)$$

Per definition, this is the inductance of the inductor, assuming infinite permeability of the core. The presented model (16) extends existing inductance models from the literature by a frequency-dependency, which is caused by the shielding effect of the foils.

IV. MODEL FOR A FINITE PERMEABILITY AND RECTANGULAR CENTRE LEGS

The presented model is derived for circular centre legs and an infinite relative permeability. In the following, corrections considering rectangular centre legs and a finite, complex permeability are introduced.

A. Rectangular centre legs

To consider centre legs with rectangular cross-sections, an appropriate length scaling of the 2D models is required. This can be achieved by multiplying the 2D fields from section II with the lengths of the straight winding sections in Cartesian coordinates. In addition, the four corners of the winding could be considered with (11) for $d_{\mathrm{leg}} = 0$.

Instead, another approach is pursued, in order to avoid additional derivations and to make use of the already obtained results from section III. A coefficient k_{rect} is defined, which links the circumferences C_{rect} of a rectangle with side lengths a_{leg} and b_{leg} to the circumference C_{circ} of a circle. Hence, it is assumed that the geometry has a rectangular cross-section with width $b_{\mathrm{leg}} = d_{\mathrm{leg}}$ and depth a_{leg}, as given in Fig. 2d). It follows:

$$k_{\mathrm{rect}} = \frac{C_{\mathrm{rect}}}{C_{\mathrm{circ}}} = \frac{4}{\pi}\left(1 + \frac{a_{\mathrm{leg}} - b_{\mathrm{leg}}}{4x}\right) \qquad (17)$$
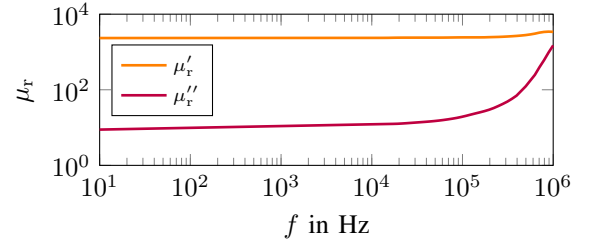

Fig. 3. Real part μ_{r}' and imaginary part μ_{r}'' of the complex permeability of the material N87, extracted from the manufacturer's data sheet [21] for $B = 25\,\mathrm{mT}$ (small signal excitation) and $T = 25\,^{\circ}\mathrm{C}$.

where x is either u_m or v_n, and a_{leg} and b_{leg} are given in Fig. 2d). Every region that is considered in the calculation must be adjusted by its respective coefficient. Since the radius of the curvature is assumed to be much greater than the thickness of the individual regions, using the inner circumference of each region for the correction is justifiable. k_{rect} is used to scale the winding losses given in (11) and the magnetic energy in (15). This way, no additional derivations must be performed and the results of the previous sections can be used to calculate the winding losses and the inductance of inductors with rectangular centre legs as well. There is no notable error induced by this procedure, as shown later in section V-A.

In addition to the length scaling, the magnetic energy stored in the air gap in (16) must be replaced with

$$W_{\mathrm{g}} = \frac{\mu_0 b_{\mathrm{leg}} a_{\mathrm{leg}} N_{\mathrm{g}} l_{\mathrm{g}}}{2}|H_{\mathrm{g}}|^2$$

which is the squared constant magnetic field from (5) integrated over the volume of the air gaps with rectangular cross-section.

B. Finite and complex permeability

Typically, in winding loss calculation $\mu_{\mathrm{r}} \to \infty$ is assumed. However, the field strength of the air gap's H-field is significantly impacted by a lower relative permeability, as later shown in section V-A. Hence, the relative permeability is introduced in the following.

It is assumed that $\mu_{\mathrm{r}} = \mu_{\mathrm{r}}' - \mathrm{j}\mu_{\mathrm{r}}''$ [22], where μ_{r}' is the real part and μ_{r}'' is the imaginary part of the complex permeability. Fig. 3 shows the complex permeability as function of the frequency for the material N87. The curves are extracted from the data sheet [21].

Furthermore, the effective magnetic path length through the core is known and denoted with l_{e}. This quantity is usually given by the manufacturer of the core or can be derived from the core geometry as described in [23]. With l_{e}, the magnetic field is [13]:

$$H_{\mathrm{g}} = k_\mu \frac{NI}{N_{\mathrm{g}} l_{\mathrm{g}}} \quad \text{with} \quad k_\mu = \frac{1}{1 + \frac{l_{\mathrm{e}}}{\mu_{\mathrm{r}} N_{\mathrm{g}} l_{\mathrm{g}}}} \qquad (18)$$

where it is assumed that the average magnetic flux densities, in the core and in the air gaps are the same and constant (c.f. Fig. 2a) $\to$ rectangular air gap region). Then, (18) replaces (5) in the derivations in section II to account for the finite permeability in the field calculations. Note, that the relative

permeability in (18) can be complex. Furthermore, the phase angles of the flux density in the core and in the air gap must be the same, with consideration of the complex permeability.

To validate the previous simplification, a 2D FEM simulation was performed with the parameters from Tab. II. The average magnetic flux densities B_c (core) and B_g (air gap without fringing field – c.f. Fig. 2a) rectangular air gap region) were calculated with

$$B = \frac{1}{A} \iint_A \hat{B} \, \mathrm{d}A$$

where $\hat{B}$ is the true and spatially inhomogeneous flux density distribution in the region of consideration. The results of the FEM simulation are $B_c = 12.42 \, \mathrm{mT}$ and $B_g = 12.33 \, \mathrm{mT}$, whereas (18) results in $12.33 \, \mathrm{mT}$, hence, the assumption is valid in this context. In general, this assumption can be applied, if the centre leg diameter is greater than the air gap length.

In addition, the magnetic energy in the core has to be taken into account, especially for a low μ_r. The magnetic energy in the core, using its effective volume V_e, is:

$$W_c = \frac{V_e}{2} B_c H_c^* = \frac{\mu_0 V_e |H_g|^2}{2\mu_r^*} \quad (19)$$

The magnetic energy (19) must be added to (16). Note, that by considering the complex permeability, (16) and (19) become complex.

V. MODEL VERIFICATION

The verification of the models is performed in two steps. First, numerous FEM simulations are conducted to identify potential error sources in detail by comparing the analytical derivations with a 2D circular symmetric FEM model in section V-A. In a second step, measurements are performed, which are compared to analytical results of the winding loss and the inductances in section V-B. In addition, Tab. I presents a pseudo-algorithm to explain the required steps, that must be followed to calculate the winding losses and the inductance with the proposed models.
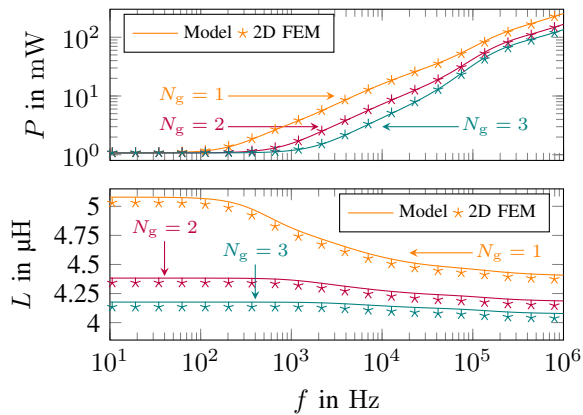
Fig. 4. Proposed winding loss and inductance models compared to 2D rotationally symetrical FEM (marked with ⋆ in the respective color) vs. frequency with constant and real-valued relative permeability, for different numbers of air gaps. The inductance decreases notably at higher frequencies due to the shielding effect.

TABLE I
CALCULATION OF R AND L WITH THE PROPOSED MODELS

In: Geometrical parameters – ω, N, N_g, h_g, h_f, d_{leg}, $d_{x,\mathrm{i}}$, d_f, d_t, $d_{x,\mathrm{o}}$.
1: function CALC_R_AND_L
2:     *% Determine air gap field (relative permeability):*
3:     $H_g \leftarrow$ Eq. (5) or (18)

4:     *% Coefficients, independent of the air gap field:*
5:     $B_{m,0}, C_{n,0}, D_{n,0} \leftarrow$ Eqs. (6), (7)

6:     *% Coefficients, based on the air gap field:*
7:     $C_{n,k}, D_{n,k}, M_{n,k}, N_{n,k} \leftarrow$ Eqs. (8), (9)

8:     *% Compute winding losses and resistance:*
9:     $P \leftarrow$ Eq. (12), if necessary Eq. (17)
10:    $R \leftarrow$ Eq. (13)

11:    *% Compute magnetic energy and inductance:*
12:    $W \leftarrow$ Eq. (15), if necessary Eqs. (17), (19)
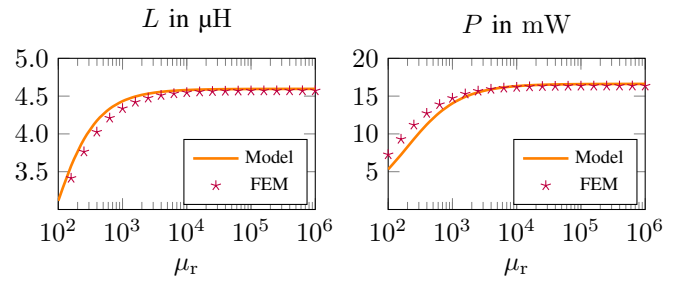13: $L \leftarrow$ Eq. (16)

Fig. 5. Comparison of proposed model results with 2D circular symmetrical FEM simulations for a fixed frequency, $N_g = 1$, and $h_g = 1 \, \mathrm{mm}$. Left: Inductance with varying relative permeability – Right: Winding losses with varying relative permeability.

At this point it should be noted, that the length scaling of the model, as derived in section III, is only valid for the special case of P-Core inductors. In general, it must be assumed that every core has a so-called 'outside window portion' (OW) [24], where no limb and no core yokes are present. In this portion of the winding, the magnetic field is not modelled properly with the proposed model. However, the error is shown to be comparatively small in [12] ($\leq 2\%$). In [25], correction factors for the reluctance of the OW paths are proposed, which can be incorporated into the model for the spatial coefficients in (8) to increase the accuracy.

A. Verification of the model via FEM

In the following, the equations for the inductance and the winding losses, derived in section III, are verified with FEM simulations. In addition, a variation of the relative permeability is investigated. Rotationally symmetrical as well as full 3D models are used. Because in reality there is a gap between the conductors and the core yokes, the actual core window height (h_w) is different from the conductor height (h_f) in the FEM simulations. The conductor height in the analytical calculations and in the FEM simulations are set to the same value. All geometrical specifications of the FEM model are given in Tab. II. Note, that all simulations are conducted at a fixed operating frequency and the conductor thickness is derived as the optimum thickness for minimum winding losses

for this frequency according to [26]. The temperature is set to $100\,°\mathrm{C}$.

Fig. 4 compares the analytical results to the results obtained with a rotationally symmetrical FEM model. It is shown, that the analytical expressions (12) and (16) match well over a wide frequency range for different numbers of air gaps. The constant overestimation of the inductance is less than $1\,\%$. It is notable, that the inductance decreases significantly with frequency, especially in the case of a single air gap. Due to the fact, that magneto-quasi-static simulations are performed with a real-valued and constant relative permeability, this can only be explained by the magnetic shielding of the foil conductors: As the frequency increases, eddy currents arise in the conductors, creating a magnetic field opposite to the air gap field, which attenuates the air gap field in the conductors. This effect counteracts the fringing field of the air gaps, resulting in an overall lower stored magnetic energy in the core window and consequently in a lower inductance. The change of inductance in Fig. 4b) is therefore fully caused by a change in magnetic energy in the core window. Analytical inductance models known from literature typically neglect the shielding effect of foil conductors [16].

Since a parametric study of varying finite permeability is difficult in reality, the respective error is investigated with FEM

simulations. Fig. 5b) and c) show the results of the proposed model computed for a varying finite permeability and of the FEM model. For $\mu_\mathrm{r} > 1000$ the model results show very good agreement with the FEM simulations. Below $\mu_\mathrm{r} = 1000$, the results still match, however, recognizable errors especially in the winding loss calculation occur ($-27\,\%$ at $\mu_\mathrm{r} = 100$). Cases, where the relative permeability is below 100, are not considered, since with such a low permeability typically no air gaps are used.

Lastly, two 3D FEM models were simulated with the parameters of Tab. II (rectangular center leg with $b_\mathrm{leg} = d_\mathrm{leg}$, $a_\mathrm{leg} = 20\,\mathrm{mm}$). The results are shown in Fig. 6. The average errors are $2.5\,\%$ for the winding loss calculation and $2.1\,\%$ for the inductance calculation in Fig. 6a), and $5.4\,\%$ for the winding loss calculation and $1.6\,\%$ for the inductance calculation in Fig. 6b). Note, that the proposed model overestimates the indutance, especially at low frequencies, with the highest error of $2.2\,\%$.

B. Verification by measurements

Two inductors based on commercially available cores – IND 1: ETD 59/31/22 [27] and IND 2: E 65/32/27 [28], as specified in Tab. III and shown in Fig. 1 – are made of the material N87 [21]. The winding is composed of foil conductors, that are wound around the centre leg without bobbin. The parameter values of the winding are obtained from measurements of the actual copper foil and the built inductors. The impedance measurement is performed with an Impedance Analyzer Keysight E4990A. The measurements were performed at room temperature.

The impedance of the inductor calculated from the proposed winding loss and inductance models is given as:

$$\underline{Z} = \left((R_\mathrm{1D} + R_\mathrm{gap} + \mathrm{j}\omega L)^{-1} + \mathrm{j}\omega C_\mathrm{res}\right)^{-1} \qquad (20)$$

where $C_\mathrm{res} = 1/((2\pi f_\mathrm{res})^2 L_\mathrm{res})$ is the static stray capacitance of the inductor obtained from a (floating core) measurement of the first resonant frequency f_res. Since the inductance is assumed to be frequency-dependent, L_res is analytically calculated instead of using a static inductance, which could

TABLE II
PARAMETERS OF THE 2D CIRCULAR SYMMETRIC FEM MODEL

|	Operating point		
I	2	A	Peak sinusoidal current
f	10	kHz	Operating frequency
	Geometrical specifications		
μ_r	5000		Relative permeability of the core
l_c	97	mm	Effective magnetic path length
V_c	22 700	mm^3	Effective magnetic volume
N	5		Number of foil conductors
h_f	26.6	mm	Conductor height
h_w	29.6	mm	Core window height
d_leg	12.2	mm	Center leg diameter
$d_{x,\mathrm{i}}$	1	mm	Distance center leg first conductor
d_w	8.65	mm	Core window width
d_f	440	µm	Conductor thickness
d_t	440	µm	Insulation thickness
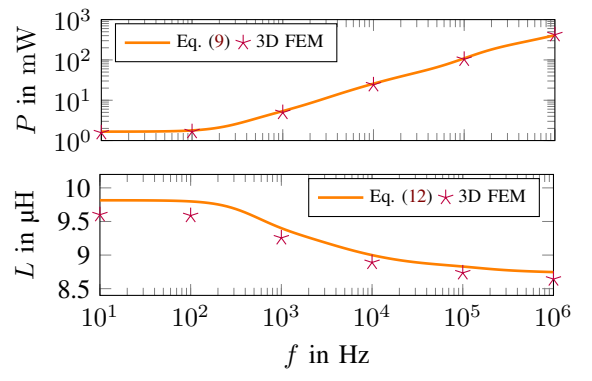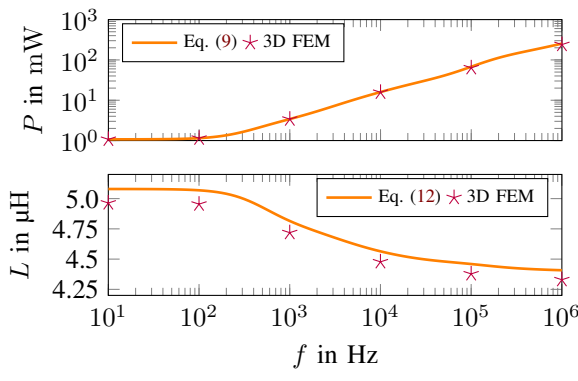
Fig. 6. Results of a 3D FEM simulation. **a)** Inductor with circular center leg according to Tab. II. **b)** Inductor according to Tab. II, but with rectangular center leg with $b_\mathrm{leg} = d_\mathrm{leg}$ and $a_\mathrm{leg} = 20\,\mathrm{mm}$. The impact of the shielding effect on the inductance is notable.
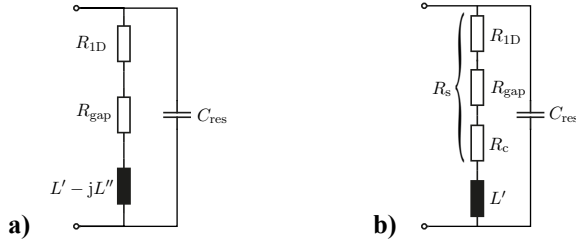
Fig. 7. Circuit diagram of the inductor used in this paper and assumed by the impedance analyzer by (20).

be obtained from a static inductance measurement. Since $\underline{L}$ in (20) is complex (consider section IV-B):

$$j\omega\underline{L} = j\omega\left(L' - jL''\right) = R_c + j\omega L'$$

where L' and L'' are the real and imaginary parts of the inductance, $\omega L'$ denotes the reactance of the RL series equivalent circuit, and

$$R_c = \omega L''$$

describes the core losses. A circuit diagram of the inductor which is used in this paper to identify the individual lumped parameters, and which is also assumed by the impedance analyzer internally, is shown in Fig. 7.

The resistance, obtained as $\Re\{\underline{Z}\}$ from (20), is compared with measurement results in Fig. 8a) and Fig. 8b). For reference, the plots show R_{1D}, R_{gap}, R_c, and their sum $R_s = R_{gap} + R_{1D} + R_c$ separately to elaborate the individual contributions of the resistance components to the inductor impedance.

To verify the inductance calculation procedure, the inductance obtained as $\Im\{\underline{Z}\}/\omega$ from (20) is compared to measured values obtained from the imaginary part of the measured impedance in Fig. 8c) and Fig. 8d). For reference, the DC inductance from the A_L-value and the inductance L from (16) are depicted.

To compare the measurements with the calculated values, it should be noted that the model is sensitive to parameter variations of $d_{x,i}$, since this parameter defines the distance of the foils to the air gap and the fringing field. In order to examine this impact more closely, calculations with the model are evaluated. IND 1 is considered, the frequency is set to 10 kHz (at very low frequencies there is no impact, because there is no shielding effect), and the model parameters are taken from Tab. III. If it is assumed that the distance $d_{x,i}$

TABLE III
MODEL PARAMETERS OF THE TWO TEST CASE INDUCTORS

	IND 1	IND 2		
C	56.6	90.0	pF	Measured capacitance
N	18	18		Number of conductors
l_g	2	3	mm	Air gap height
h_f	40	40	mm	Conductor height
d_{leg}	22.1		mm	Center leg diameter
a_{leg}		27.4	mm	Center leg diameter
b_{leg}		20.0	mm	Center leg diameter
$d_{x,i}$	350	450	µm	See Fig. 2
d_f	100	100	µm	Conductor thickness

deviates from 350 µm by ±150 µm, a variation in resistance of -8.7 % / 9.9 % and a variation in inductance of 1.4 % / -1.5 % can be observed, respectively. If the original value of $d_{x,i}$ is changed from 350 µm to 2 mm and again a variation of 150 µm is assumed, variations in resistance of -5.0 % / 5.5 % and variation in inductance of 0.6 % / -0.6 % can be observed.

C. Discussion of the results

The results in Fig. 8a) and b) indicate, that at least one major effect influencing the effective resistance of the inductors is not considered correctly in the modelling. This becomes evident at frequencies above 300 kHz. Given the results of section V-A, the error appears due to either the capacitance or the core loss modelling. Above 300 kHz, the relative permeability increases significantly, as shown in Fig. 3, causing the core losses to increase as well. However, the chosen approach to take the core losses into account could be less accurate in the high-frequency range. Furthermore, the significant change of the complex permeability for frequencies above 300 kHz [29] influences not only the losses but also the inductance. Therefore, at the first resonant frequency, which was measured at 2.37 MHz for IND 1 and 1.90 MHz and IND 2, respectively, the inductance may have changed significantly, leading to an erroneous estimation of the capacitance C_{res}.

The comparison of the effective layer resistance R_{1D}, equivalent to [3] and the air gap resistance R_{gap} reveals that the air gap fringing field has a huge impact on the overall resistance. The reason can be found in the comparatively large expansion of the conductors in y-direction, which is much larger than the expansion in x-direction. Hence, the magnetic field can extend inside the foil in y-direction relatively unhindered, resulting in a significant increase of eddy currents and thus, the effective resistance. This fact supports the hypothesis, that foil conductors perform poorly in the vicinity of air gaps [7].

The average error of the calculated resistance compared to the measurement in Fig. 8a) for frequencies from 1 kHz to 300 kHz is -14.0 % (in the range of -14.5 % to -13.2 %), and the error of the calculated resistance in the same frequency range in Fig. 8b) is between -4.5 % and 6.2 % and the average error is 2.2 %. In this frequency range, the additional core losses and capacitive effects are not significant and the comparison of the proposed model with the measurements is possible. As indicated by the results of section V-A, the calculation of accurate results with the proposed winding loss and inductance models is not limited to a certain frequency range. The errors in Fig. 8 depends on additional effects, such as the capacitance, or dimensional and frequency effects in the core, such as a strongly inhomogeneous flux density distribution.

Special attention should be paid to the inductance model that is proposed in this paper. Fig. 8c) and Fig. 8d) show, that the measured inductance decreases significantly with the frequency. Since the inductance is directly proportional to the real part of the complex permeability [29], which does not change in the relevant frequency range as shown in Fig. 3, this change is not caused by a change of the relative permeability.

Overall, the model matches the measured inductance well. As already established in section V-A, the inductance model
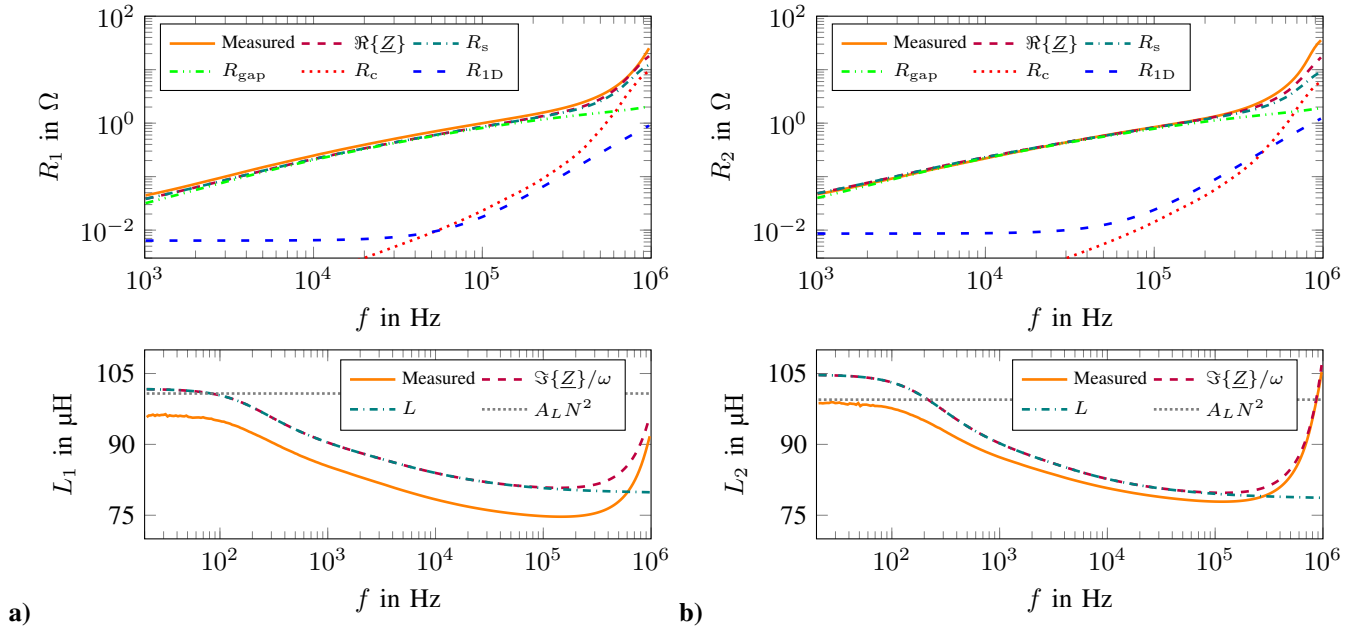
Fig. 8. Comparison of the calculated inductance and effective resistance and an impedance measurement of IND 1 in **a)** and the same for IND 2 in **b)**.

TABLE IV
COMPARISON OF DIFFERENT INDUCTANCE CALCULATION METHODS:
ERROR IN PERCENT COMPARED TO THE MEASURED INDUCTANCE FOR
DIFFERENT FREQUENCIES

f in Hz	25	10^3	10^4	10^5	25	10^3	10^4	10^5
		IND 1				IND 2		
M1	5.8	5.9	7.1	8.1	5.9	3.4	2.4	2.4
M2	-25.3	-15.9	-8.4	-4.0	-28.5	-19.1	-12.6	-9.4
M3	3.6	16.6	27.0	33.0	2.5	16.0	25.3	30.0
M4	13.9	28.1	39.6	46.2	17.5	33.0	43.8	49.1
M5	4.9	18.0	28.6	34.7	0.7	14.0	23.2	27.7

tends to slightly overestimate the inductance, which is reflected also in the measurements. However, since the A_L-value from the manufacturer's datasheet also shows this offset, the error is possibly subject to manufacturing tolerances (e.g. the relative permeability of the core is lower than the value given by the manufacturer, the air gap is slightly larger, etc. . .). On the other hand, the A_L-value and the measurement match well in the case of IND 2 (Fig. 8d), whereas the proposed model shows inaccuracies, especially at low frequencies. Here, the model inaccuracies may be introduced by the correction factor for rectangular centre legs, which does not consider edge effects where the conductors are tightly bent around the core edges, as explained in section III.

For comparison with the proposed model, different methods from literature are used to compute the inductance. The methods are the standard procedure using a reluctance network of the core [30] without considering the fringing effect or the shielding effect (M2), the method by McLyman [14] to empirically consider the fringing effect (M3), the Schwarz-Christoffel approach [17] to analytically consider the 3D fringing effect (M4), and the manufacturers A_L-value (M5). The proposed model is denoted with M1. The relative error of each method compared to the measurement results is shown

in Tab. IV. As expected, all modelling approaches except for M1 show significant errors at high frequencies, since they all neglect the shielding effect. However, the results are unexpected, because M4, which is expected to be accurate at low frequencies, shows a significant error. It is found that model M4 shows errors of this magnitude for comparatively large air gaps, which is especially the case with IND 2. The same is true for the empirical correction factor of M3. This can be verified using the manufacturers A_L-value. Both models tend to overestimate the inductance for comparatively large air gaps but are relatively accurate for small air gaps.

Nevertheless, the measurements show that the proposed model is accurate in the complete recommended operating frequency range of the material, especially considering the shielding effect of the foil conductors and the decreased inductance, that comes with it. The average error of the proposed model for all considered cases in Tab. IV is 5.1 %.

D. Additional notes on the measurements

To avoid variations of the measured values, the Impedance Analyzer was configured to measure 5 values per frequency point and take the average of those values. In addition, multiple frequency sweeps were performed. The capacitance was measured with a floating core.

Regarding measurement accuracy, errors must be expected. From [31], it can be concluded that the overall measurement error is below 1 % between 1 kHz and 1 MHz and below 5 % as long as $f > 20$ Hz, when measuring the impedance with the given inductor specifications. In addition, since the impedance is mostly inductive, the resistance measurement is prone to higher errors. Therefore, the results of the resistance measurement are shown in a narrower frequency range (1 kHz and 1 MHz) only, to keep the error as low as possible.

All measurements are performed with sinusoidal small-signal excitation. Therefore, the relative permeability of the

core material is modelled as frequency-dependent only. In reality, the permeability depends non-linearly on the operating point, considering DC-bias, saturation, and the dynamic position in the B-H loop during operation, as well as the temperature. Larger deviations of the actual winding resistance compared to the calculated winding resistance must be expected [32], since the proposed modelling approach is not capable of capturing these effects. It is therefore recommended to use different models [33] to account for the additional core losses.

VI. Conclusion

This paper derives an analytical model for the magnetic field inside the core window of gapped inductors with foil windings. The resulting expressions allow to analytically calculate the inductance and the total winding losses, caused by skin, proximity, and fringing effects. The resulting model is capable of precisely predicting the expected winding losses and the inductance of a gapped inductor with foil windings over a wide frequency range, considering especially the influence of the air gaps. The average error is below $15\,\%$.

In addition, it is shown, that the inductance of a gapped inductor with foil windings is frequency-dependent, which is caused by the shielding effect of the foil conductors. As a result, the inductance decreases by appr. $20\,\%$ compared to the DC value, which is also proven by measurements. The proposed model considers this effect and shows improved accuracy compared to existing inductance models for gapped inductors, with an average error of $5\,\%$ over a wide frequency range.

Acknowledgment

References

[1] J. Biela, J. W. Kolar, A. Stupar, U. Drofenik, and A. M. Musing, "Towards virtual prototyping and comprehensive multi-objective optimisation in power electronics," in *Int. Exhib. & Conf. for Power Electronics Intelligent Motion Power Quality (PCIM)*, May 2010.

[2] J. Muehlethaler, "Modeling and multi-objective optimization of inductive power components," Ph.D. dissertation, Eidgenössische Technische Hochschule (ETH) Zürich, 2012.

[3] P. L. Dowell, "Effects of eddy currents in transformer windings," in *Proc. of the Institution of Electrical Engineers*, vol. 113, no. 8, Aug. 1966, pp. 1387–1394.

[4] M. Bartoli, A. Reatti, and M. Kazimierczuk, "Minimum copper and core losses power inductor design," in *Conf. Rec. of the 31st Ind. App. Conf. (IAS)*. IEEE, 1996.

[5] A. Rahimi-Kian, A. Keyhani, and J. Powell, "Minimum loss design of a 100 kHz inductor with litz wire," in *Conf. Rec. of the 32nd Ind. App. Conf. (IAS)*. IEEE, 1997.

[6] M. Kazimierczuk and H. Sekiya, "Design of AC resonant inductors using area product method," in *Energy Conversion Congress and Exposition*. IEEE, Sep. 2009.

[7] D. Leuenberger and J. Biela, "Semi-numerical method for loss calculation in foil windings exposed to an air gap field," in *Proc. Int. Power Electronics Conference (IPEC)*, May 2014.

[8] I. Kovačević-Badstübner, R. Burkart, C. Dittli, J. W. Kolar, and A. Musing, "A fast method for the calculation of foil winding losses," in *17th European Conf. on Power Electronics and Applications (EPE ECCE Europe)*, Sep. 2015.

[9] A. Van den Bossche and V. Valchev, "Eddy current losses and inductance of gapped foil inductors," in *28th Annu. Conf. IEEE Industrial Electronics Society (IECON)*, Nov. 2002.

[10] P. Wallmeier, N. Frohleke, and H. Grotstollen, "Improved analytical modeling of conductive losses in gapped high-frequency inductors," in *33rd IEEE Industry Applications Society Conf. (IAS)*, vol. 2, Oct. 1998, pp. 913–920.

[11] W. Zhang and T. M. Jahns, "Analytical 2-d slot model for predicting ac losses in bar-wound machine windings due to armature reaction," in *IEEE Transportation Electrification Conf. and Expo. (ITEC)*, Jun. 2014.

[12] T. Ewald and J. Biela, "Analytical eddy current loss model for foil conductors in gapped cores," *23th European Conference on Power Electronics and Applications (EPE ECCE Europe)*, Aug. 2021.

[13] W. G. Hurley and W. H. Wölfle, *Transformers and Inductors for Power Electronics - Theory, Design and Applications*. John Wiley & Sons, Ltd, 2013.

[14] C. McLyman, *Transformer and Inductor Design Handbook*. CRC Press, 2017.

[15] A. Van den Bossche, V. Valchev, and T. Filchev, "Improved approximation for fringing permeances in gapped inductors," in *Record of the 37th Industry Applications Conf.* IEEE, 2002.

[16] A. Balakrishnan, W. T. Joines, and T. G. Wilson, "Air-gap reluctance and inductance calculations for magnetic circuits using a schwarz-christoffel transformation," *IEEE Transactions on Power Electronics*, vol. 12, no. 4, pp. 654–663, July 1997.

[17] J. Muehlethaler, J. W. Kolar, and A. Ecklebe, "A novel approach for 3d air gap reluctance calculations," in *8th International Conference on Power Electronics (ECCE Asia)*, May 2011.

[18] L. O. Fichte, S. Lange, T. Steinmetz, and M. Clemens, "Shielding properties of a conducting bar calculated with a boundary integral method," *Advances in Radio Science*, vol. 3, pp. 119–123, may 2005.

[19] J. D. Jackson, *Klassische Elektrodynamik*. DE GRUYTER, 2013.

[20] M. Albach, *Induktivitäten in der Leistungselektronik*. Springer Vieweg, Wiesbaden, 2017.

[21] *Ferrites and Accessories - SIFERRIT Material N87*, TDK, Sep. 2017.

[22] M. Kazimierczuk, *High Frequency Magnetic Components*. John Wiley & Sons, Ltd, 2013.

[23] E. Snelling, *Soft ferrites: properties and applications*. Newnes-Butterworth, 1969.

[24] J. Muehlethaler, J. W. Kolar, and A. Ecklebe, "Loss modeling of inductive components employed in power electronic systems," in *8th Int. Conf. Power Electronics*, May 2011, pp. 945–952.

[25] A. F. Hoke and C. R. Sullivan, "An improved two-dimensional numerical modeling method for e-core transformers," in *APEC. Seventeenth Annual IEEE Applied Power Electronics Conference and Exposition (Cat. No.02CH37335)*, vol. 1, 3 2002.

[26] W. Hurley, E. Gath, and J. Breslin, "Optimizing the AC resistance of multilayer transformer windings with arbitrary current waveforms," *IEEE Transactions on Power Electronics*, vol. 15, no. 2, pp. 369–376, mar 2000.

[27] *Ferrites and Accessories - ETD 59/31/22*, TDK, May 2017.

[28] *Ferrites and Accessories - E 65/32/27*, TDK, Apr. 2018.

[29] T. P. Todorova, A. V. den Bossche, and V. C. Valchev, "A procedure for the extraction of intrinsic AC conductivity and dielectric constant of n87 mn–zn ferrite samples based on impedance measurements and equivalent electrical circuit modeling," *IEEE Transactions on Power Electronics*, vol. 33, no. 12, pp. 10 723–10 735, Dec. 2018.

[30] V. C. Valchev and A. V. den Bossche, *Inductors and Transformers for Power Electronics*. CRC Press, Taylor & Francis Group, 2005.

[31] *Keysight E4990A Impedance Analyzer*, Keysight, 2018.

[32] B. X. Foo, A. L. F. Stein, and C. R. Sullivan, "A step-by-step guide to extracting winding resistance from an impedance measurement," in *Applied Power Electronics Conference and Exposition (APEC)*. IEEE, Mar. 2017.

[33] K. Venkatachalam, C. Sullivan, T. Abdallah, and H. Tacca, "Accurate prediction of ferrite core loss with nonsinusoidal waveforms using only steinmetz parameters," in *Workshop on Computers in Power Electronics*. IEEE, Jun. 2002.

Thomas Ewald (Student Member, IEEE) studied electrical engineering with focus on Energy Conversion Technology at Technical University of Munich (TUM) in Germany. He received his B.Sc. and M.Sc. degree from TUM in 2015 and 2018, respectively. In 2017, he wrote his Master's Thesis at BMW AG in the R&D department for electrical drive components. In his Master's thesis he developed an analytical model for simulating transient processes in both, permanent magnet and electrically excited synchronous machines. Since November 2019 he is a Ph.D. student at the Laboratory for High Power Electronic Systems (HPE) at ETH Zurich, working on analytical inductor models and automated optimization processes.

Jürgen Biela (Senior Member, IEEE) received the Diploma (hons.) degree from Friedrich-Alexander Universität Erlangen-Nürnberg, Erlangen, Germany, in 1999, and the Ph.D. degree from the Swiss Federal Institute of Technology (ETH), Zürich, Switzerland, in 2006. In 2000, he joined the Research Department, Siemens A&D, Erlangen, and in 2002, he joined the Power Electronic Systems Laboratory, ETH Zürich, as a Ph.D. Student focusing on electromagnetically integrated resonant converters, where he was a Postdoctoral Fellow from 2006 to 2010. Since 2010, he has been an Associate Professor, and since 2020, a Full Professor of high-power electronic systems with ETH Zurich.